JACS
JOURNAL OF THE AMERICAN CHEMICAL SOCIETY
Article
pubs.acs.org/JACS

Self-Templated Formation of Interlaced Carbon Nanotubes Threaded Hollow Co_3S_4 Nanoboxes for High-Rate and Heat-Resistant Lithium–Sulfur Batteries

Tao Chen,[†] Zewen Zhang,[†] Baorui Cheng,[†] Renpeng Chen,[†] Yi Hu,[†] Lianbo Ma,[†] Guoyin Zhu,[†] Jie Liu,*[,†,‡] and Zhong Jin*[,†]

[†]Key Laboratory of Mesoscopic Chemistry of MOE and Collaborative Innovation Center of Chemistry for Life Sciences, School of Chemistry and Chemical Engineering, Nanjing University, Nanjing, Jiangsu 210023, PR China

[‡]Department of Chemistry, Duke University, Durham, North Carolina 27708, United States

Supporting Information

ABSTRACT: Lithium–sulfur batteries (Li–S) have attracted soaring attention due to the particularly high energy density for advanced energy storage system. However, the practical application of Li–S batteries still faces multiple challenges, including the shuttle effect of intermediate polysulfides, the low conductivity of sulfur and the large volume variation of sulfur cathode. To overcome these issues, here we reported a self-templated approach to prepare interconnected carbon nanotubes inserted/wired hollow Co_3S_4 nanoboxes (CNTs/Co_3S_4–NBs) as an efficient sulfur host material. Originating from the combination of three-dimensional CNT conductive network and polar Co_3S_4–NBs, the obtained hybrid nanocomposite of CNTs/Co_3S_4–NBs can offer ultrahigh charge transfer properties, and efficiently restrain polysulfides in hollow Co_3S_4–NBs via the synergistic effect of structural confinement and chemical bonding. Benefiting from the above advantages, the S@CNTs/Co_3S_4–NBs cathode shows a significantly improved electrochemical performance in terms of high reversible capacity, good rate performance, and long-term cyclability. More remarkably, even at an elevated temperature (50 °C), it still exhibits high capacity retention and good rate capacity.

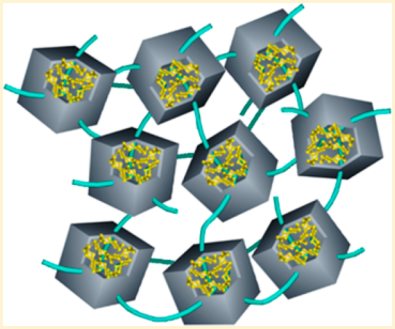

INTRODUCTION

In the past two decades, rechargeable lithium ion batteries have been successfully used in many applications, such as consumer electronics and electrical vehicles. Nevertheless, the energy density of traditional lithium ion batteries (less than 400 Wh kg^{-1} for $LiCoO_2$/graphite cells) cannot satisfy the rapidly growing demand of portable electronics.[1−4] Therefore, there is an urgent need to develop alternative energy storage systems with higher energy density and longer cyclic life. Lithium–sulfur (Li–S) batteries have become one of most promising candidates for next-generation energy storage devices due to its overwhelming theoretical energy density (~2600 Wh kg^{-1}), low cost and environmental friendliness.[5−8] However, there are some intractable obstacles hindering the commercialization of Li–S batteries:[9−11] First, the poor conductivity of sulfur and Li_2S/Li_2S_2 restricts the electron transport in the sulfur cathode and the utilization of the active sulfur. Second, the dissolution of lithium polysulfides (Li_2S_x, $4 \le x \le 8$) in the electrolytes gives rise to low Coulombic efficiency and short cycle life. Third, the large volume change of sulfur during charge–discharge process causes the pulverization of sulfur cathode and results in a rapid capacity decay. In the past decade, tremendous efforts have been devoted to develop carbonaceous sulfur hosts, such as porous carbon,[12−17] carbon nanotubes/nanofibers,[18−22] graphene,[23−28] and hollow carbon nanospheres.[29,30] However, owing to the weak van der Waals interaction between nonpolar carbon and polar polysulfide species, only physical confinement is not sufficient to suppress the shuttle effect of polysulfides over long-term cycling, inevitably causing fast capacity decay.[31] Therefore, carbonaceous materials alone cannot be viewed as ideal choice of sulfur host.

Recently, it has been reported that the chemical interaction between polar nanomaterials and lithium polysulfides can dramatically strengthen the absorption and thus alleviate the shuttle effect. These materials include metal oxides,[32−42] sulfides,[43−46] MXenes,[47,48] and conductive polymers.[49−51] However, the poor electrical conductivity of most metal oxides/sulfides trends to slow down the redox kinetics of absorbed polysulfides, resulting in low utilization of sulfur and rate capability. Recent researches indicate that incorporating the polar nanocrystals or nanosheets of conductive polar materials into porous or hollow carbon frameworks should be a feasible strategy to significantly enhance the conductivity of sulfur cathode and prevent the dissolution of polysulfides.[52−55] Meanwhile, the high-temperature tolerance of Li–S batteries is also important for the demands of practical applications, because high temperatures can aggravate the lithium polysulfide dissolution into electrolyte and lead to poor cyclability;[56] however, there are very few literatures concerning this aspect.

Received: July 6, 2017
Published: August 24, 2017

DOI: 10.1021/jacs.7b06973
J. Am. Chem. Soc. 2017, 139, 12710−12715

Therefore, it is important to design advanced sulfur hosts based on hybrid nanostructures of conductive polar materials and nanocarbons with high polysulfide-trapping capability for maximizing the cycling life, rate performance and heat resistance of Li−S batteries.

According to this line of thinking, it can be deduced that an ideal nanostructural sulfur host should have the following merits: (1) large free space and a closed structure for storing sulfur species and buffering volumetric expansion; (2) strong affinity or interactions with sulfur species to prevent the dissolution of polysulfides; (3) smooth Li^+ and electron pathways to promote the redox kinetics; (4) high local conductivity and an integrative conductive network for improving sulfur utilization and rate performance.

To fulfill these requirements, here we report a novel sulfur host material based on interlaced carbon nanotubes threaded hollow Co_3S_4 nanoboxes (CNTs/Co_3S_4−NBs) that can greatly improve the overall performance of sulfur cathode. The Co_3S_4 in spinel group exhibits attractive metallic nature with a remarkable room-temperature conductivity of 3.3×10^3 S cm^{-1}.[57] The conductive and polar Co_3S_4−NBs have large inner space for sulfur storage, and can effectively suppress the shuttle effect by the chemical binding/absorption with polysulfides, meanwhile ensuring fast charge transport to promote redox reaction. Furthermore, the interlaced CNTs inserted/threaded into Co_3S_4−NBs can provide an integrative conductive network that facilitate the electron transport all-over the electrode (especially the sulfur species encapsulated in Co_3S_4−NBs), thus greatly improving the sulfur utilization rate and rate capability. The unique hybrid nanostructure of CNTs/Co_3S_4−NBs is very conducive to the trapping and cyclical utilization of internal lithium polysulfides for the overall capacity contribution. With these merits, the obtained sulfur-filled CNTs/Co_3S_4−NBs (S@CNTs/Co_3S_4−NBs) cathodes can deliver high discharge capacity, remarkable rate performance and impressive cycling stability, much superior to the control sample of simple sulfur-filled Co_3S_4−NBs without interlaced CNTs (S@Co_3S_4−NBs), as illustrated in Scheme 1. More importantly, even at raised temperature of 50 °C, stable cycling performance with high capacity retention can still be achieved after long-term tests.

Scheme 1. Structural Advantages of S@CNTs/Co_3S_4−NBs Cathode over S@Co_3S_4−NBs Cathode during Charge−Discharge Processes

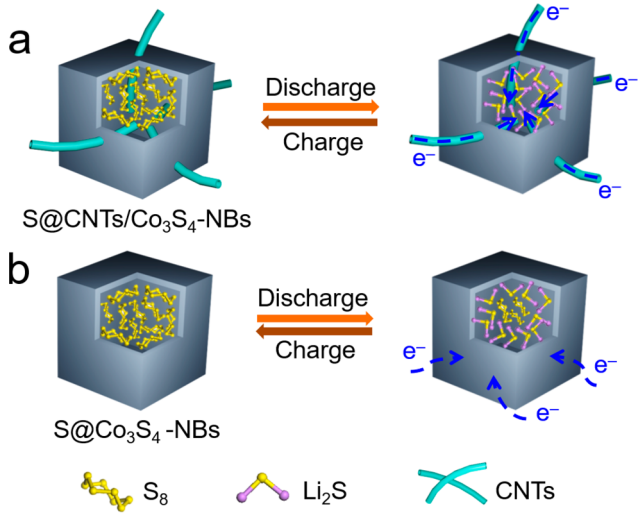

RESULTS AND DISCUSSION

The S@CNTs/Co_3S_4−NBs composite was prepared using CNTs threaded zeolitic imidazolate framwwork-67 (CNTs/ZIF-67) as precursor via a facile self-templated approach, as schematically illustrated in Figure 1a. Details of the synthesis

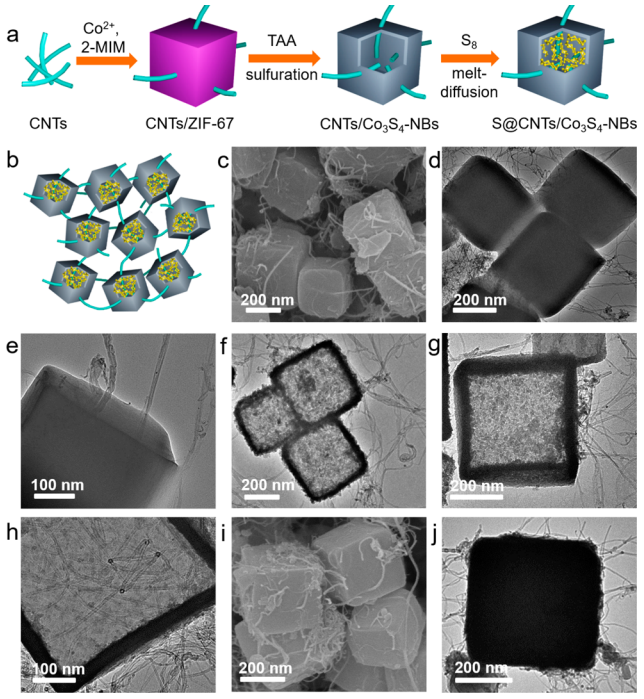

Figure 1. (a) Schematic illustration of the synthesis process of S@CNTs/Co_3S_4−NBs. (b) the schematic diagram of the three-dimensional interlaced CNT conductive network formed in S@CNTs/Co_3S_4−NBs. (c) SEM and (d,e) TEM images of CNTs/ZIF-67 precursor. (f−h) TEM images of CNTs/Co_3S_4−NBs. (i) SEM and (j) TEM images of as-obtained S@CNTs/Co_3S_4−NBs after the filling of sulfur.

steps can be found in the experimental section. Briefly, uniformed ZIF-67 nanocubes were in situ nucleated and grown on well-dispersed CNTs functionalized with carboxyl groups (−COOH) to form CNTs/ZIF-67 precursor. Afterward, the CNTs/ZIF-67 was chemically transformed to CNTs/Co_3S_4−NBs hybrid structure via solvothermal sulfuration and subsequent thermal annealing. The formation of hollow Co_3S_4−NBs is mainly ascribed to the Kirkendall effect originated from the different diffusion rates of cobalt and sulfur species (Scheme S1). Finally, sulfur was filled into CNTs/Co_3S_4−NBs via a melt-diffusion method to obtain S@CNTs/Co_3S_4−NBs.[58] Figure 1b shows the schematic diagram of integrative three-dimensional conductive network formed in the S@CNTs/Co_3S_4−NBs. The morphological features of as-synthesized CNTs/ZIF-67 precursor and CNTs/Co_3S_4−NBs were characterized by scanning electron microscopy (SEM) and transmission electron microscopy (TEM). As shown in Figure 1c, the ZIF-67 nanocubes with an average size of about 450 nm were grown and threaded in the CNT network. Figure 1d,e clearly exhibits that the CNTs are successfully inserted into the ZIF-67 nanocubes. Figure 1f shows TEM images of the CNTs/Co_3S_4−NBs, presenting hollow structure of Co_3S_4−NBs. The shells of hollow Co_3S_4−NBs are composed of dense ultrafine Co_3S_4 nanocrystals, with an average thickness of ~20 nm (Figure 1g). It also can be observed that many carbon

DOI: 10.1021/jacs.7b06973
J. Am. Chem. Soc. 2017, 139, 12710−12715

nanotubes are successfully filled/inserted in Co_3S_4–NBs (Figure 1h). Energy-dispersive X-ray spectroscopy (EDX) revealed a Co/S atomic ratio of ~0.74, consistent with the stoichiometric ratio of Co_3S_4 (Figure S1a). Accordingly, the content of Co_3S_4 in the CNTs/Co_3S_4–NBs was calculated to be ~86.9 wt %. After the filling of sulfur, the as-obtained S@CNTs/Co_3S_4–NBs well preserved the original size and morphology of the CNTs/Co_3S_4–NBs, and no sulfur particles are observed on the outer surface (Figure 1i). TEM image reveals that most inner cavity of the S@CNTs/Co_3S_4–NBs was filled by sulfur (Figure 1j). EDX analysis further confirms the existence of Co, C and S elements, and the high atomic ratio of S indicates a large amount of sulfur encapsulated in the S@CNTs/Co_3S_4–NBs (Figure S1b). The elemental mappings and linear-scanning energy-dispersive X-ray spectroscopy (EDS) analysis (Figure 2) show the existence and spatial distribution of Co, S, and C elements in S@CNTs/Co_3S_4–NBs, further confirming the encapsulation of sulfur in the CNTs/Co_3S_4–NBs host.

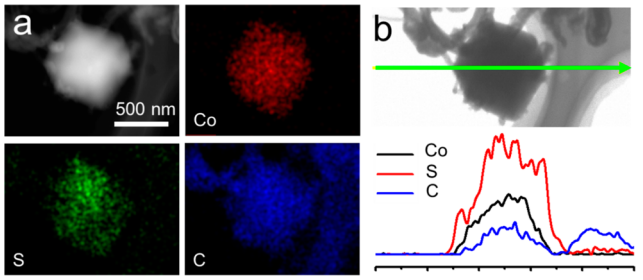

Figure 2. (a) High-angle annular dark-field scanning TEM (HAADF-STEM) image and corresponding elemental mapping images of S@CNTs/Co_3S_4–NBs. (b) TEM image of S@CNTs/Co_3S_4–NBs and corresponding EDS line-scanning curves of Co, S, and C elements.

To compare with CNTs/Co_3S_4–NBs composite, pristine Co_3S_4–NBs and sulfur-filled Co_3S_4–NBs (S@Co_3S_4–NBs) in the absence of interlaced CNTs were also prepared as control samples (Figure S2). The X-ray diffraction (XRD) patterns of S@CNTs/Co_3S_4–NBs, CNTs/Co_3S_4–NBs, pristine Co_3S_4–NBs, and CNTs/ZIF-67 are shown in Figure 3a. The XRD pattern of CNTs/ZIF-67 shows high crystallinity, and the weak peak at around 26.4° can be assigned to the (002) plane of the interlaced CNTs. The crystal phase of the Co_3S_4–NBs control sample only shows pure cubic Co_3S_4 (JCPDS No. 47–1738). The XRD pattern of CNTs/Co_3S_4–NBs shows the characteristic peak of CNTs (26.4°) in addition to the peaks of Co_3S_4. Strong peaks of orthorhombic sulfur (JCPDS No.08–0247) in the XRD pattern of S@CNTs/Co_3S_4–NBs indicate the presence of elemental sulfur. The weight ratio of sulfur in S@CNTs/Co_3S_4–NBs was determined to be ~70 wt % according to thermogravimetric analysis (TGA), as shown in Figure 3b. The pore structures of the CNTs/Co_3S_4–NBs and S@CNTs/Co_3S_4–NBs were identified by nitrogen absorption–desorption isotherm (Figure 3c,d). The CNTs/ZIF-67 precursor has a high BET surface area of 1956 $m^2\ g^{-1}$ and abundant micropores with an average diameter of ~1.4 nm calculated by the nonlocal density functional theory (NLDFT) method (Figure S3). The CNTs/Co_3S_4–NBs show a Brunauer–Emmett–Teller (BET) specific surface area of 134 $m^2\ g^{-1}$, and a total pore volume of 1.3 $cm^3\ g^{-1}$. The pore size distribution of CNTs/Co_3S_4–NBs calculated by the Barrett–Joyner–Halenda (BJH) method indicates a mesoporous

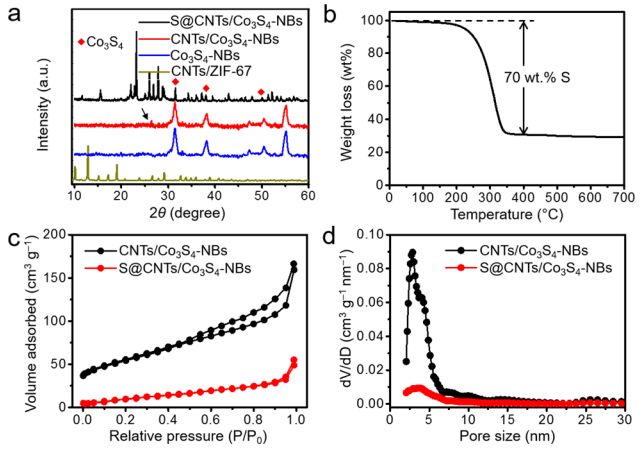

Figure 3. (a) XRD patterns of S@CNTs/Co_3S_4–NBs, CNTs/Co_3S_4–NBs, and pristine Co_3S_4–NBs. The characterize peak positions of Co_3S_4 are labeled by red dots. (b) TGA curve of S@CNTs/Co_3S_4–NBs. (c) N_2 adsorption–desorption isotherm curves of CNTs/Co_3S_4–NBs and S@CNTs/Co_3S_4–NBs. (d) Pore size distributions of CNTs/Co_3S_4–NBs and S@CNTs/Co_3S_4–NBs.

structure in a range between 2.8–10 nm. After the filling of sulfur, the BET surface area and pore volume of S@CNTs/Co_3S_4–NBs decreased to 23 $m^2\ g^{-1}$ and 0.18 $cm^3\ g^{-1}$. The remaining mesopores around 2–8 nm may originate from the inner space of CNTs. Moreover, the interlaced CNTs threaded into/between Co_3S_4–NBs can increase the electrode/electrolyte contact area (especially for the internal deep-seated sulfur species) and provide more open channels for electrolyte infiltration.

To identify the polysulfide adsorption ability of the sample, Li_2S_4@CNTs/Co_3S_4–NBs composite was prepared as a control sample (as detailed in the experimental section), and X-ray photoelectron spectroscopy (XPS) was conducted to investigate the chemical interaction between Li_2S_4 and Co_3S_4. Figure S4 show the XPS spectra at the Co $2p_{3/2}$ region of CNTs/Co_3S_4–NBs and Li_2S_4@CNTs/Co_3S_4–NBs, respectively. The Co $2p_{3/2}$ spectrum of CNTs/Co_3S_4–NBs shows two deconvoluted peaks at 779.3 and 780.8 eV, corresponding to Co^{3+} and Co^{2+}, respectively. After the adsorption of Li_2S_4, the Co $2p_{3/2}$ band of Li_2S_4@CNTs/Co_3S_4–NBs shows an overall shift toward higher binding energy, indicating the strong interaction between Li_2S_4 and Co atoms. The XPS results confirm that the CNTs/Co_3S_4–NBs can strongly bind with polysulfides via the chemical adsorption of Co_3S_4–NBs.

As another control sample, the composite of homogeneously mixed sulfur and CNTs with the same sulfur loading ratio (S@CNTs) was also prepared. The electrochemical impedance spectroscopy (EIS) spectra of the S@CNTs/Co_3S_4–NBs, S@Co_3S_4–NBs and S@CNTs electrodes are shown in Figure 4a. The high-frequency semicircles and low-frequency sloping lines in the Nyquist plots are ascribed to the charge transfer resistance (R_{ct}) and the Li^+ diffusion resistance within the electrodes, respectively. The S@CNTs/Co_3S_4–NBs electrode shows the lowest R_{ct} value (R_{ct} = 95 Ω) when compared with S@Co_3S_4–NBs (R_{ct} = 110 Ω) and S@CNTs (R_{ct} = 135 Ω). The EIS data suggest that the unique architecture of S@CNTs/Co_3S_4–NBs cathode is conducive to the Li^+ diffusion capability and electrode kinetics.

Figure 4b shows the typical charge–discharge voltage profiles of the S@CNTs/Co_3S_4–NBs, S@Co_3S_4–NBs and S@CNTs

DOI: 10.1021/jacs.7b06973
J. Am. Chem. Soc. 2017, 139, 12710–12715

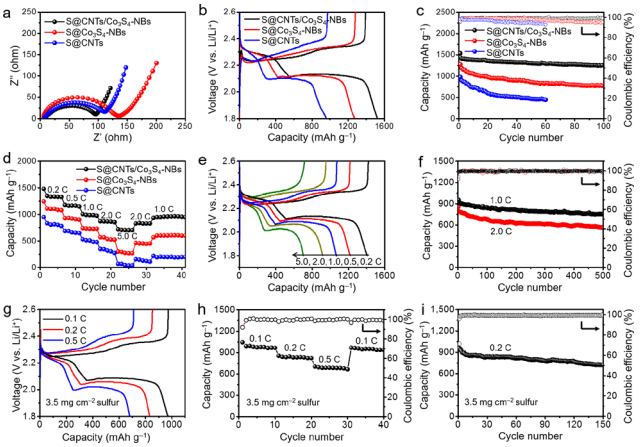

Figure 4. (a) EIS curves, (b) galvanostatic charge−discharge voltage profiles at 0.2 C, (c) cycling performances at 0.2 C, (d) rate capabilities of S@CNTs/Co_3S_4−NBs, S@Co_3S_4−NBs and S@CNTs electrodes. (e) Voltage profiles of S@CNTs/Co_3S_4−NBs electrode at various current densities between 0.2−5.0 C. (f) Long-term cycle performances of S@CNTs/Co_3S_4−NBs electrode at 1.0 and 2.0 C. (g) Voltage profiles, (h) rate capacities at various current densities from 0.1 C (0.35 mA cm^{-2}) to 0.5 C (1.75 mA cm^{-2}), and (i) cycling performance at 0.2 C (0.70 mA cm^{-2}) of S@Co_3S_4/CNTs electrode with high sulfur areal loading of 3.5 mg cm^{-2}.

electrodes at 0.2 C (1.0 C = 1,675 mAh g^{-1}). The S@CNTs/Co_3S_4−NBs electrode exhibits two typical discharge plateaus at 2.35 and 2.08 V (vs Li^+/Li), originated from the reduction of S_8 to soluble long-chain polysulfides (Li_2S_x, $4 \le x \le 8$) and the formation of insoluble short-chain polysulfides (Li_2S/Li_2S_2), respectively. The single charge plateau of S@CNTs/Co_3S_4−NBs between 2.25−2.36 V is ascribed to the oxidation of Li_2S/Li_2S_2 to Li_2S_x and eventually S_8. These charge and discharge plateaus are consistent with corresponding CV curves (Figure S5). Notably, the S@CNTs/Co_3S_4−NBs electrode exhibits lower potential hysteresis and higher sulfur utilization ratio than those of the S@Co_3S_4−NBs and S@CNTs, mainly attributed to the strong chemical affinity of polar Co_3S_4−NBs with polysulfides and the interconnected CNT network.

The cycling performances of the samples were measured at a current density of 0.2 C, as shown in Figure 4c. Benefit from the high loading and utilization ratio of sulfur, the S@CNTs/Co_3S_4−NBs cathode exhibits a high initial discharge capacity of 1535 mAh g^{-1} and keeps at 1254 mAh g^{-1} after 100 cycles, corresponding to an average capacity decay rate of merely 0.18% per cycle. In contrast, the S@Co_3S_4−NBs cathode presents a discharge capacity of 771 mAh g^{-1} after 100 cycles, and the S@CNTs cathode shows a capacity of only 442 mAh g^{-1} after 60 cycles, owing to the rapid dissolution of polysulfides into the electrolyte. The capacity decay rate of CNTs/Co_3S_4−NBs is much lower than those of S@Co_3S_4−NBs and S@CNTs, demonstrating the structural advantages in trapping polysulfides. Moreover, the Coulombic efficiency of S@CNTs/Co_3S_4−NBs electrode maintains at more than 99%, indicating that the remarkable cyclic stability. These results prove that the combination of hollow Co_3S_4−NBs and interlaced CNT conductive network can provide effective confinement and chemical absorption with polysulfides, and form smooth pathways for Li^+ and electron transport, thus beneficial to the utilization of sulfur and the inhibition of shuttle effect.

The rate capability comparison of S@CNTs/Co_3S_4−NBs, S@Co_3S_4−NBs, S@CNTs, and S@mixed-CNTs&Co_3S_4−NBs (the sulfur composite of simply mixed CNTs and Co_3S_4−NBs) is shown in Figure 4d and Figure S6. When cycled at 0.2, 0.5, 1.0, 2.0, and 5.0 C, the S@CNTs/Co_3S_4−NBs cathode can deliver impressive discharge capacities of 1330, 1165, 988, 859, and 702 mAh g^{-1}, respectively. As the current density turns back to 1.0 C, the discharge capacity of S@CNTs/Co_3S_4−NBs restores to 958 mAh g^{-1}, indicating good structural stability at high rate. In contrast, the discharge capacities of S@Co_3S_4−NBs cathode fades sharply from 1240 to 268 mAh g^{-1} when the rate increases from 0.2 to 2.0 C. What is more, the discharge capacity of S@CNTs fades dramatically to 37 mAh g^{-1} when the current rate increases to 5.0 C. It is clear that the S@CNTs/Co_3S_4−NBs cathode exhibits much higher rate capabilities than those of S@Co_3S_4−NBs and S@CNTs. The galvanostatic charge−discharge voltage profiles of the S@CNTs/Co_3S_4−NBs cathode at various current rates were also measured (Figure 4e). The results confirm that the incorporation of interlaced CNT network is very helpful to improve the rate capability of S@CNTs/Co_3S_4−NBs. Moreover, the localized and overall electron transfer of the sulfur species trapped in S@CNTs/Co_3S_4−NBs can be effectively facilitated by the interconnected CNT network inserted in and threaded between the Co_3S_4−NBs (Figure S7).

The long-term cycling performance of S@CNTs/Co_3S_4−NBs electrode was also tested at high rates of 1.0 and 2.0 C for 500 cycles (Figure 4f). At 1.0 C, the S@CNTs/Co_3S_4−NBs cathode delivers an initial discharge capacity of 954 mAh g^{-1} and retains a discharge capacity of 752 mAh g^{-1} after 500 cycles. The capacity decay is as low as 0.042% per cycle with a high Coulombic efficiency of over 99.2%. Remarkably, at a higher rate of 2.0 C, the S@CNTs/Co_3S_4−NBs cathode delivers an initial discharge capacity of 858 mAh g^{-1} and a high reversible capacity of 565 mAh g^{-1} after 500 cycles with a capacity decay of only 0.068% per cycle, benefited from the effective confinement of polysulfides within the polar and hollow Co_3S_4−NBs.

The areal loading mass of sulfur and the electrolyte volume/sulfur weight (E/S) ratio are viewed as two key parameters for the energy density of practical Li−S batteries.[59−61] Therefore, thick electrodes of S@CNTs/Co_3S_4−NBs with high sulfur loading mass of 3.5 mg cm^{-2} were tested (Figure S8). As shown in Figure 4g,h, the thick S@CNTs/Co_3S_4−NBs electrode shows remarkable rate capability with discharge capacities of 978 mAh g^{-1} (3.42 mAh cm^{-2}), 835 mAh g^{-1} (2.92 mAh cm^{-2}), and 685 mAh g^{-1} (2.40 mAh cm^{-2}) at 0.1 C, 0.2 and 0.5 C, respectively. Moreover, when the rate turned back to 0.1 C, a stable discharge capacity of 950 mAh g^{-1} (3.32 mAh cm^{-2}) was recovered. Figure 4i shows the cycling stability of thick S@CNTs/Co_3S_4−NBs cathode at 0.2 C. When cycled at 0.2 C, an initial capacity of 1012 mAh g^{-1} is achieved, corresponding to an areal capacity of 3.54 mAh cm^{-2}. After 150 cycles, the electrode still retains a reversible capacity of 820 mAh g^{-1} (2.87 mAh cm^{-2}), and shows average Coulombic efficiency of ≥99% during the cycling process, indicating the high cycling stability even with high sulfur loading weight. Notably, the S@CNTs/Co_3S_4−NBs electrode in this work exhibit very competitive areal capacities and cycling stability compared to other existing metal- chalcogenide based composite cathodes (Table S1).

To further reveal the cyclability enhancement mechanism of S@CNTs/Co_3S_4−NBs cathode, the coin cells with S@CNTs/Co_3S_4−NBs, S@ Co_3S_4−NBs and S@CNTs cathodes were

DOI: 10.1021/jacs.7b06973
J. Am. Chem. Soc. 2017, 139, 12710−12715

disassembled in fully discharged state after 30 cycles at 0.2 C. The three cathodes were separately immersed into a mixture of 1,3-dioxolane (DOL) and 1,2-dimethoxyethane (DME) (1:1 in volume) for 4 h. As shown in Figure 5a, the color of the

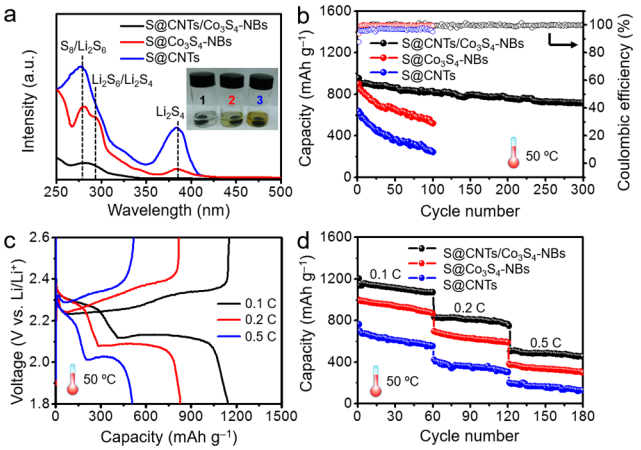

Figure 5. (a) UV−vis absorption spectra collected from the DOL/DME mixed solutions soaked with (1) S@CNTs/Co_3S_4−NBs, (2) S@Co_3S_4−NBs and (3) S@CNTs cathodes after 30 cycles at 0.2 C, respectively. The inset photograph shows the color comparison of the solutions containing the corresponding electrodes. (b) Cyclic performance of S@CNTs/Co_3S_4−NBs, S@Co_3S_4−NBs and S@CNTs electrodes at 0.2 C under 50 °C. (c) Voltage profiles and (d) rate capacities of S@CNTs/Co_3S_4−NBs S@Co_3S_4−NBs and S@CNTs electrodes at 0.1 C, 0.2 and 0.5 C under 50 °C, respectively.

solution containing S@CNTs/Co_3S_4−NBs cathode is almost transparent, suggesting the low leakage of polysulfides into electrolyte. In comparison, the solutions soaked with S@Co_3S_4−NBs or S@CNTs cathodes turned to yellow, indicating the large amount of dissolved sulfur species. Besides the direct visual comparison, UV−vis absorption spectra were also collected for investigating the suppression degree of shuttle effect. In the fully discharged state after 30 cycles, the solutions immersed with S@Co_3S_4−NBs or S@CNTs cathodes show obvious light absorption peaks around 280, 292, and 384 nm, attributed to the dissolution of S_8/Li_2S_6, Li_2S_6/Li_2S_4 and Li_2S_4, respectively. In contrast, the solution soaked with S@CNTs/Co_3S_4−NBs cathode shows much weaker light absorption peaks, and the peak around 384 nm (corresponding to the dissolved Li_2S_4) is negligible, indicating that the S@CNTs/Co_3S_4−NBs cathode can effectively accelerate the polysulfide redox reaction and meanwhile suppress the shuttling effect during cycling.

The heat resistance of Li−S batteries is very important for the safety in practical applications. The thermal endurance of Li−S batteries not only relies on the compositions of electrolyte (Table S2), but also the architecture and compositions of cathodes, because the rationally designed cathodes can effectively restrict the dissolution of lithium polysulfides into the electrolyte and reduce the electrolyte consumption at raised temperatures (Table S3). To identify the high-temperature endurance, the S@CNTs/Co_3S_4−NBs cathode was tested at an elevated temperature of 50 °C (Figure 5b), showing an initial discharge capacity of 953 mAh g^{-1} at 0.2 C. After 300 cycles, the discharge capacity was stabilized at 718 mAh g^{-1} with a capacity retention of 75.3%, suggesting remarkable cycling stability at high temperature. In contrast, the S@Co_3S_4−NBs cathode shows a much lower discharge capacity of 515 mAh g^{-1} after 100 cycles at 50 °C. Moreover, the S@CNTs/Co_3S_4−NBs cathode also shows impressive rate capability at high temperature (Figure 5c,d). When cycled at 0.1, 0.2, and 0.5 C over 60 cycles, the discharge capacities of S@CNTs/Co_3S_4−NBs are measured to be 1058, 765, and 446 mAh g^{-1}, respectively, showing a high-temperature stability much superior to the S@Co_3S_4−NBs and S@CNTs cathode. Compared with other previously reported cathodes for heat-resistant Li−S batteries (Table S3), the S@CNTs/Co_3S_4−NBs cathode shows very competitive cycling stability and rate capability at elevated temperature.

CONCLUSION

In summary, we have designed and prepared a novel hybrid sulfur host composed of hollow Co_3S_4−NBs inserted/threaded with interlaced CNTs. In this unique nanostructure, the polar Co_3S_4−NBs provide effective confinement of polysulfides and serve as nanosized electrochemical reaction chambers to restrict the outward diffusion. The CNTs embedded in Co_3S_4−NBs form a highly conductive network for rapid charge transfer, resulting in high sulfur utilization and good rate performance. The remarkable performance of S@CNTs/Co_3S_4−NBs cathode has been determined in terms of high reversible capacity, good rate capability, long cycling stability, high areal capacity and high-temperature endurance. We expect this work may open up an effective route to construct advanced hybrid sulfur host materials for achieving high-performance Li−S batteries.

ASSOCIATED CONTENT

Supporting Information

The Supporting Information is available free of charge on the ACS Publications website at DOI: 10.1021/jacs.7b06973.

Experimental details, supplementary characterization methods including EDX spectra, SEM, TEM, and other electrochemical measurement (PDF)

AUTHOR INFORMATION

Corresponding Authors

*j.liu@duke.edu

*zhongjin@nju.edu.cn

ORCID

Tao Chen: 0000-0003-2536-4145

Jie Liu: 0000-0003-0451-6111

Zhong Jin: 0000-0001-8860-8579

Notes

The authors declare no competing financial interest.

ACKNOWLEDGMENTS

This work was supported by National Key Research and Development Program of China (2017YFA0208200, 2016YFB0700600), National Key Basic Research Program (2015CB659300), Projects of NSFC (21403105, 21573108), China Postdoctoral Science Foundation (2015M580413, 2015M581769), Natural Science Foundation for Young Scholars of Jiangsu Province (BK20150583, BK20160647), Fundamental Research Funds for the Central Universities (020514380107) and a project funded by the Priority Academic Program Development of Jiangsu Higher Education Institutions.

DOI: 10.1021/jacs.7b06973
J. Am. Chem. Soc. 2017, 139, 12710−12715

REFERENCES

(1) Yang, Y.; Zheng, G. Y.; Cui, Y. *Chem. Soc. Rev.* **2013**, *42*, 3018.
(2) Bruce, P. G.; Freunberger, S. A.; Hardwick, L. J.; Tarascon, J.-M. *Nat. Mater.* **2012**, *11*, 19.
(3) Manthiram, A.; Chung, S.-H.; Zu, C. *Adv. Mater.* **2015**, *27*, 1980.
(4) Tarascon, J. M.; Armand, M. *Nature* **2001**, *414*, 359.
(5) Zhou, G.; Paek, E.; Hwang, G. S.; Manthiram, A. *Nat. Commun.* **2015**, *6*, 7760.
(6) Sun, J.; Sun, Y.; Pasta, M.; Zhou, G.; Li, Y.; Liu, W.; Xiong, F.; Cui, Y. *Adv. Mater.* **2016**, *28*, 9797.
(7) Yu, M. P.; Ma, J. S.; Song, H. Q.; Wang, A. J.; Tian, F. Y.; Wang, Y. S.; Qiu, H.; Wang, R. M. *Energy Environ. Sci.* **2016**, *9*, 1495.
(8) Rehman, S.; Khan, K.; Zhao, Y. F.; Hou, Y. L. *J. Mater. Chem. A* **2017**, *5*, 3014.
(9) Seh, Z. W.; Li, W.; Cha, J. J.; Zheng, G.; Yang, Y.; McDowell, M. T.; Hsu, P. C.; Cui, Y. *Nat. Commun.* **2013**, *4*, 1331.
(10) Liang, Z.; Zheng, G.; Li, W.; Seh, W. Z.; Yao, H.; Yan, K.; Kong, D.; Cui, Y. *ACS Nano* **2014**, *8*, 5249.
(11) Lee, T. J.; Zhao, Y.; Thieme, S.; Kim, H.; Oschatz, M.; Borchardt, L.; Magasinski, A.; Cho, W.-I.; Kaskel, S.; Yushin, G. *Adv. Mater.* **2013**, *25*, 4573.
(12) Song, J.; Gordin, L. M.; Xu, T.; Chen, S.; Yu, Z.; Sohn, H.; Lu, J.; Ren, Y.; Duan, Y.; Wang, D. *Angew. Chem., Int. Ed.* **2015**, *54*, 4325.
(13) Schuster, J.; He, G.; Mandlmeier, B.; Yim, T.; Lee, T. K.; Bein, T.; Nazar, F. L. *Angew. Chem., Int. Ed.* **2012**, *51*, 3591.
(14) Ji, X. L.; Lee, K. T.; Nazar, L. F. *Nat. Mater.* **2009**, *8*, 500.
(15) Liang, J.; Sun, Z.-H.; Li, F.; Cheng, H.-M. *Energy Storage Mater.* **2016**, *2*, 76.
(16) Elazari, R.; Salitra, G.; Garsuch, A.; Panchenko, A.; Aurbach, D. *Adv. Mater.* **2011**, *23*, 5641.
(17) Rehman, S.; Gu, X. X.; Khan, K.; Mahmood, N.; Yang, W. L.; Huang, X. X.; Guo, S. J.; Hou, Y. L. *Adv. Energy Mater.* **2016**, *6*, 1502518.
(18) Yu, M. L.; Wang, Z. Y.; Wang, Y. W.; Dong, Y. F.; Qiu, J. S. *Adv. Energy Mater.* **2017**, 1700018.
(19) Zheng, G.; Zhang, Q.; Cha, J. J.; Yang, Y.; Li, W.; Seh, W. Z.; Cui, Y. *Nano Lett.* **2013**, *13*, 1265.
(20) Yao, H.; Zheng, G.; Li, W.; McDowell, M. T.; Seh, W. Z.; Liu, N.; Lu, Z.; Cui, Y. *Nano Lett.* **2013**, *13*, 3385.
(21) Sun, L.; Li, M. Y.; Jiang, Y.; Kong, W. B.; Jiang, K. L.; Wang, J. P.; Fan, S. S. *Nano Lett.* **2014**, *14*, 4044.
(22) Pu, X.; Yang, G.; Yu, C. *Adv. Mater.* **2014**, *26*, 7456.
(23) Lu, S.; Cheng, Y.; Wu, X.; Liu, J. *Nano Lett.* **2013**, *13*, 2485.
(24) Wang, H.; Yang, Y.; Liang, Y.; Robinson, J. T.; Li, Y.; Jackson, A.; Cui, Y.; Dai, H. *Nano Lett.* **2011**, *11*, 2644.
(25) Zhang, M. D.; Yu, C.; Yang, J.; Zhao, C. T.; Ling, Z.; Qiu, J. S. *J. Mater. Chem. A* **2017**, *5*, 10380.
(26) Liu, Y.; Wang, X. Z.; Dong, Y. F.; Tang, Y. C.; Wang, L. X.; Jia, D. Z.; Zhao, Z. B.; Qiu, J. S. *Chem. Commun.* **2016**, *52*, 12825.
(27) Wang, Z. Y.; Dong, Y. F.; Li, H. J.; Zhao, Z. B.; Wu, H. B.; Hao, C.; Liu, S. H.; Qiu, J. S.; Lou, X. W. *Nat. Commun.* **2014**, *5*, 5002.
(28) Gu, X. X.; Tong, C. J.; Lai, C.; Qiu, J. X.; Huang, X. X.; Yang, W. L.; Wen, B.; Liu, L. M.; Hou, Y. L.; Zhang, S. Q. *J. Mater. Chem. A* **2015**, *3*, 16670.
(29) Jayaprakash, N.; Shen, J.; Moganty, S. S.; Corona, A.; Archer, L. A. *Angew. Chem., Int. Ed.* **2011**, *50*, 5904.
(30) Zhang, C. F.; Wu, H. B.; Yuan, C. Z.; Guo, Z. P.; Lou, X. W. *Angew. Chem., Int. Ed.* **2012**, *51*, 9592.
(31) Zhang, Q. F.; Wang, Y. P.; Seh, Z. W.; Fu, Z. H.; Zhang, R. F.; Cui, Y. *Nano Lett.* **2015**, *15*, 3780.
(32) Ji, X.; Evers, S.; Black, R.; Nazar, L. F. *Nat. Commun.* **2011**, *2*, 325.
(33) Zhang, J.; Shi, Y.; Ding, Y.; Zhang, W.; Yu, G. *Nano Lett.* **2016**, *16*, 7276.
(34) Hwang, J. Y.; Kim, H. M.; Lee, S. K.; Lee, J. H.; Abouimrane, A.; Khaleel, M. A.; Belharouak, I.; Manthiram, A.; Sun, Y. K. *Adv. Energy Mater.* **2016**, *6*, 1501480.
(35) Yao, H. B.; Zheng, G. Y.; Hsu, P. C.; Kong, D. S.; Cha, J. J.; Li, W. Y.; Seh, Z. W.; McDowell, M. T.; Yan, K.; Liang, Z.; Narasimhan, V. K.; Cui, Y. *Nat. Commun.* **2014**, *5*, 3943.
(36) Liang, X.; Kwok, C. Y.; Lodi-Marzano, F.; Pang, Q.; Cuisinier, M.; Huang, H.; Hart, C. J.; Houtarde, D.; Kaup, K.; Sommer, H.; Brezesinski, T.; Janek, J.; Nazar, J. F. *Adv. Energy Mater.* **2016**, *6*, 1501636.
(37) Liang, X.; Hart, C.; Pang, Q.; Garsuch, A.; Weiss, T.; Nazar, L. F. *Nat. Commun.* **2015**, *6*, 5682.
(38) Li, Z.; Zhang, J.; Lou, X. W. *Angew. Chem., Int. Ed.* **2015**, *54*, 12886.
(39) Wang, X.; Li, G.; Li, J.; Zhang, Y.; Wook, A.; Yu, A.; Chen, Z. *Energy Environ. Sci.* **2016**, *9*, 2533.
(40) Tao, Y.; Wei, Y.; Liu, Y.; Wang, J.; Qiao, W.; Ling, L.; Long, D. *Energy Environ. Sci.* **2016**, *9*, 3230.
(41) Rehman, S.; Guo, S. J.; Hou, Y. L. *Adv. Mater.* **2016**, *28*, 3167.
(42) Rehman, S.; Tang, T. Y.; Ali, Z.; Huang, X. X.; Hou, Y. L. *Small* **2017**, *13*, 1700087.
(43) Seh, Z. W.; Yu, J. H.; Li, W. Y.; Hsu, P.-C.; Wang, H. T.; Sun, Y. M.; Yao, H. B.; Zhang, Q. F.; Cui, Y. *Nat. Commun.* **2014**, *5*, 5017.
(44) Yuan, Z.; Peng, H. J.; Hou, T. Z.; Huang, J. Q.; Chen, C. M.; Wang, D. W.; Cheng, X. B.; Wei, F.; Zhang, Q. *Nano Lett.* **2016**, *16*, 519.
(45) Zhang, S.; Tran, D. T. *J. Mater. Chem. A* **2016**, *4*, 4371.
(46) Lei, T. Y.; Chen, W.; Huang, J. W.; Yan, C. Y.; Sun, H. X.; Wang, C.; Zhang, W. L.; Li, Y. R.; Xiong, J. *Adv. Energy Mater.* **2017**, *7*, 1601843.
(47) Liang, X.; Garsuch, A.; Nazar, L. F. *Angew. Chem., Int. Ed.* **2015**, *54*, 3907.
(48) Liang, X.; Rangom, Y.; Kwok, C. Y.; Pang, Q.; Nazar, L. F. *Adv. Mater.* **2017**, *29*, 1603040.
(49) Xiao, L. F.; Cao, Y. L.; Xiao, J.; Schwenzer, B.; Engelhard, M. H.; Saraf, L. V.; Nie, Z. M.; Exarhos, G. J.; Liu, J. *Adv. Mater.* **2012**, *24*, 1176.
(50) Yang, Y.; Yu, G. H.; Cha, J. J.; Wu, H.; Vosgueritchian, M.; Yao, Y.; Bao, Z. N.; Cui, Y. *ACS Nano* **2011**, *5*, 9187.
(51) Dong, Y. F.; Liu, S. H.; Wang, Z. Y.; Liu, Y.; Zhao, Z. B.; Qiu, J. S. *Nanoscale* **2015**, *7*, 7569.
(52) Pang, Q.; Kundu, D.; Cuisinier, M.; Nazar, L. F. *Nat. Commun.* **2014**, *5*, 4759.
(53) Pang, Q.; Kundu, D.; Nazar, L. F. *Mater. Horiz.* **2016**, *3*, 130.
(54) Sun, Z. H.; Zhang, J. Q.; Yin, L. C.; Hu, G. J.; Fang, R. P.; Cheng, H.-M.; Li, F. *Nat. Commun.* **2017**, *8*, 14627.
(55) Li, Z.; Zhang, J. T.; Guan, B. Y.; Wang, D.; Liu, L.-M.; Lou, X. W. *Nat. Commun.* **2016**, *7*, 13065.
(56) Li, X.; Lushington, A.; Sun, Q.; Xiao, W.; Liu, J.; Wang, B. Q.; Ye, Y. F.; Nie, K. Q.; Hu, Y. F.; Xiao, Q. F.; Li, R. Y.; Guo, J. H.; Sham, T.-K.; Sun, X. L. *Nano Lett.* **2016**, *16*, 3545.
(57) Bouchard, R. J.; Russo, P. A.; Wold, A. *Inorg. Chem.* **1965**, *4*, 685.
(58) Lee, J. S.; Kim, W.; Jang, J.; Manthiram, A. *Adv. Energy Mater.* **2017**, *7*, 1601943.
(59) Klein, M. J.; Veith, G. M.; Manthiram. *J. Am. Chem. Soc.* **2017**, *139*, 9229.
(60) Pang, Q.; Liang, X.; Kwok, C. Y.; Kulisch, J.; Nazar, L. F. *Adv. Energy Mater.* **2017**, *7*, 1601630.
(61) Shyamsunder, A.; Beichel, W.; Klose, P.; Pang, Q.; Scherer, H.; Hoffmann, A.; Murphy, G. K.; Krossing, I.; Nazar, L. F. *Angew. Chem., Int. Ed.* **2017**, *56*, 6192.

DOI: 10.1021/jacs.7b06973
J. Am. Chem. Soc. 2017, 139, 12710−12715